

<https://doi.org/10.1038/s43247-024-01389-5>

The early Cretaceous was cold but punctuated by warm snaps resulting from episodic volcanism

Check for updates

Lee Nordt¹ ✉, Daniel Breecker² & Joseph White³

The Cretaceous is characterized as a greenhouse climate from elevated atmospheric carbon dioxide concentrations, transgressive seas, and temperate ecosystems at polar paleolatitudes. Here we test the hypothesis that the early Cretaceous was a cold climate state with a new Aptian atmospheric carbon dioxide record from the C₃ plant proxy and early Cretaceous sea level curve from stable oxygen isotopes of belemnites and benthic foraminifera. Results show that carbon dioxide concentrations were persistently below 840 ppm during the Aptian, validating recent General Circulation Model simulations of ice sheets on Antarctica at those concentrations. In addition, sea level was estimated to be within the ice sheet window for much of the early Cretaceous prior to the Albian. This background state appears to have been episodically interrupted by Large Igneous Province volcanism followed by long-term carbon burial from weathering. We hypothesize that the early Cretaceous was largely an icehouse punctuated by warm snaps.

The Cretaceous (143.1–66.0 Ma) is typically characterized as a greenhouse climate extrapolated from elevated atmospheric carbon dioxide (CO₂) concentrations, transgressive seas, and thermophilic biota at high latitudes^{1–3}. To the contrary, some marine isotopic indicators⁴, sea surface temperatures⁵, terrestrial glacial markers⁶, General Circulation Model (GCM) simulations⁷ and rapid sea level oscillations⁸ suggest the presence of ‘cold snaps’ during the early Cretaceous (143.1–100.5 Ma). A possible mechanism for these colder intervals includes CO₂ drawdown associated with carbon burial during ocean anoxic events (OAE) or following large igneous province (LIP) emplacement⁹.

While atmospheric CO₂ concentrations force temperature fluctuations that regulate ice sheet dynamics, CO₂ proxy data reported from the early Cretaceous are problematic because of large or unknown uncertainties and inconsistent results among the various proxies¹⁰ (Fig. 1a; Supplementary Data 1). For example, most CO₂ concentration mean values from the stomata proxy plot within the ice sheet window, many paleosol values outside of the ice sheet window, and liverwort values near the ice sheet line. Alkenones have been used to estimate CO₂ during the OAE 1a, and are thus high. The GEOCARBSULF geochemical model simulations on 1 myr time steps show CO₂ at concentrations below 840 ppm¹¹ that is within the realm of ice sheet formation shown and predicted by GCM simulations⁷ (Fig. 1b). Carbon dioxide concentrations from the COPSE geochemical model follow the ice sheet/ice-free line¹². Glacial indicators on land are sparse during the early

Cretaceous, but if widespread, tillites would be most likely buried beneath the modern Antarctic ice sheet. Biotic records in polar regions are so scarce and poorly dated that they cannot resolve the timing of short-term cold or warm snaps¹³.

Previous proxy sea level estimates through the early Cretaceous show wide ranging results⁸. The sequence boundary approach suggests a net rise during the early Cretaceous of ~160 m¹⁴, while sediment back stripping applied to the tectonically stable Russian Plateau indicates a sea level rise of only 90 m¹⁵. (Fig. 1c). However, both sea level curves, regardless of magnitude, exhibit sea level shifts on short time scales consistent with possible glacial-eustasy. In contrast, Phanerozoic temperature maps developed from paleo-climate indicators suggest that global temperatures were too high during the early Cretaceous to support ice sheets³.

To reconcile these paleo-climate ambiguities we tested for the possible presence of Antarctic ice sheets during the early Cretaceous by first reconstructing CO₂ concentrations from the C₃ plant proxy and by reconstructing sea level curve from a δ¹⁸O proxy of marine organisms during the Aptian. This time interval contained an abundance of available data for analysis within a temporally detailed framework. We then reconstructed sea level for the early Cretaceous from the same methods as above in the absence of reliable CO₂ proxy data. These curves were then compared to the distribution of OAEs and Large Igneous Provinces (LIPs) as possible causal mechanisms. Our results show that low atmospheric CO₂

¹Department of Geosciences, Baylor University, Waco, TX, USA. ²Department of Geological Sciences, University of Texas, Austin, TX, USA. ³Department of Biology, Baylor University, Waco, TX, USA. ✉e-mail: lee_nordt@baylor.edu

concentrations and sea level, along with glacial indicators such as tillites and glendonites, support the presence of small to large ice sheets in southern polar regions during much of the early Cretaceous, which briefly melted in response to episodic volcanism.

Results

Atmospheric CO₂ concentrations

To test the hypothesis that atmospheric CO₂ concentrations were low enough to sustain glaciers during the early Cretaceous, we applied both the C₃ plant proxy¹⁶ and the proxy for the magnitude of isotopic excursion between atmospheric and terrestrial environments $\Delta(\text{CIE}_{\text{wood}}-\text{CIE}_{\text{atm}})$ ¹⁷ to previously published data from the Aptian Stage (Methods; Supplementary Note 1). The C₃ plant proxy is based on experimental work showing an inverse relationship (parabolic) between atmospheric CO₂ concentration and the $\delta^{13}\text{C}$ of C₃ plants. The $\Delta(\text{CIE}_{\text{wood}}-\text{CIE}_{\text{atm}})$ proxy derives from the magnitude of carbon isotope excursions through mass balance considerations (Methods).

The C₃ plant proxy, aimed at quantifying paleoatmospheric CO₂ concentrations, requires that the $\delta^{13}\text{C}$ of atmospheric CO₂ and the $\delta^{13}\text{C}$ of a plant substrate be known and comparable between the time of interest and

an appropriate datum¹⁸. Violation of these parameters may lead to spurious results from differences in plant species and moisture availability¹⁹. Some researchers have proposed that plants during the Aptian were not responsive to CO₂ concentrations based on relatively high organic $\delta^{13}\text{C}$ values²⁰. To mitigate this concern, we reconstructed maximum baseline CO₂ prior to two carbon isotope excursions during the Aptian using the $\Delta(\text{CIE}_{\text{wood}}-\text{CIE}_{\text{atm}})$ proxy.

To construct the Aptian $\delta^{13}\text{C}$ atmospheric CO₂ ($\delta^{13}\text{C}_{\text{atm}}$) curve for the C₃ plant proxy, we applied carbonate equilibria reactions on bulk carbonate $\delta^{13}\text{C}$ and $\delta^{18}\text{O}$ values from Deep Sea Drilling Project (DSDP) 463 in the open ocean south Pacific (Figs. 2, 3a–c; Supplementary Data 2). The initial age model for this core was developed by ammonite zonation and Stage boundaries from GTS 2020²¹ where the Aptian stratigraphic record is thicker than most other localities in the western Tethys (e.g., Apticore) and contains the full negative CIE of approximately –4‰ during ocean anoxic event 1a (OAE 1a). Several other localities in the Pacific show bulk carbonate $\delta^{13}\text{C}$ and $\delta^{18}\text{O}$ trends and magnitudes similar to DSDP 463, suggesting the preservation of a global atmospheric $\delta^{13}\text{C}$ signal (Supplementary Fig. 1).

For the vegetation component of the C₃ plant proxy, we compiled $\delta^{13}\text{C}$ values from previously published gymnosperm wood from the Isle of

Fig. 1 | Key climate indicators of the early Cretaceous. **a** Proxy atmospheric CO₂ estimates from paleosol carbonate (gray circles), plant stomata (black circles), liverworts (white triangles) and marine alkenones (white squares) with 1 standard deviation range¹⁰. **b** Geochemical models with GEOCARBSULF¹¹ (solid) and COPSE¹² (dashed) with 16th and 84th percentile uncertainty lines. The ice sheet/ice free line shown in both panels is approximately 840 ppm from GCM simulations⁷. **c** Sea level curves from sediment backstripping with partially computed uncertainty range of 5–10 m (not shown)¹⁵, and from sequence boundary stratigraphy with no uncertainty provided¹⁴.

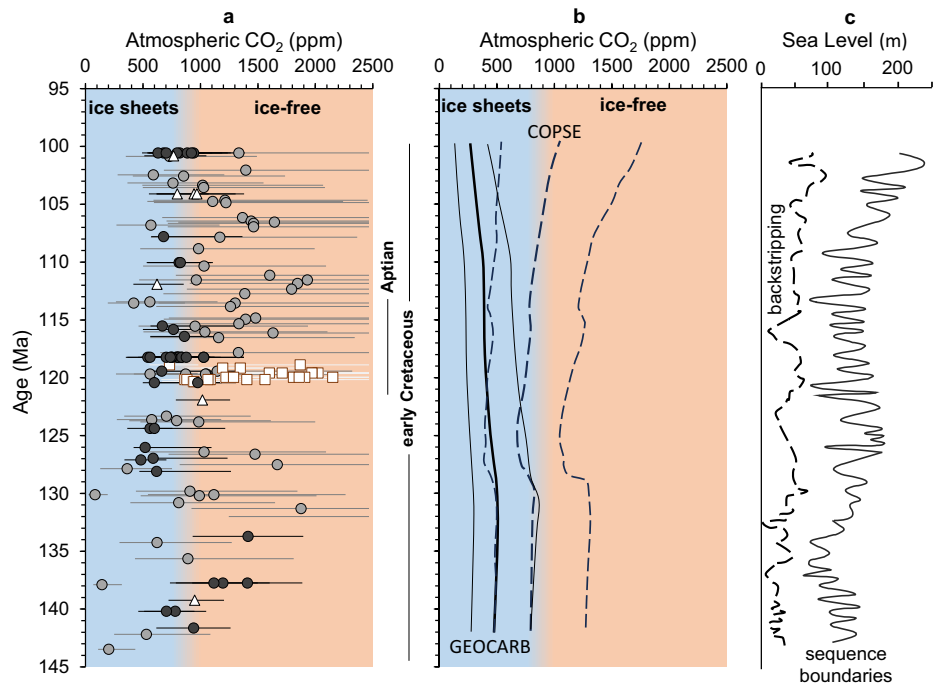
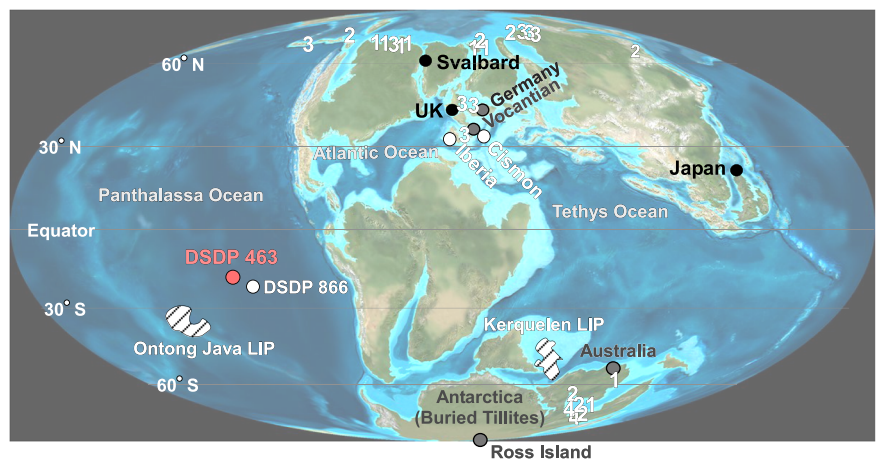


Fig. 2 | Palaeogeographic map of the Barremian-Aptian and reference locations for the early Cretaceous. Plate tectonic Maps and Continental Drift Animations by C.R. Scotese, PALEOMAP Project (www.Scotese.Com). Bulk carbonate $\delta^{13}\text{C}$ and $\delta^{18}\text{O}$ values from DSDP 463 (red circle) for computing $\delta^{13}\text{C}_{\text{atm}}$ and three $\delta^{13}\text{C}$ wood localities (black circles) for computing CO₂ from the C₃ plant proxy. Additional bulk carbonate $\delta^{13}\text{C}$ and $\delta^{18}\text{O}$ localities (white circles) for comparison to DSDP 463 (Supplementary Fig. 1). Locations shown for four belemnite $\delta^{18}\text{O}$ study areas (gray circles) to reconstruct sea level [Ross Island^{67,68}; Australia⁶⁹; Germany³⁴; Vocontian Basin⁹]. White numbers as glacial indicators: 1 – glendonites⁴; 2 – dropstones⁷⁰; 3 – dropstones⁷¹; 4 – tillites⁷². Some map locations taken from⁷³. Note presence of two LIPs active at the time.



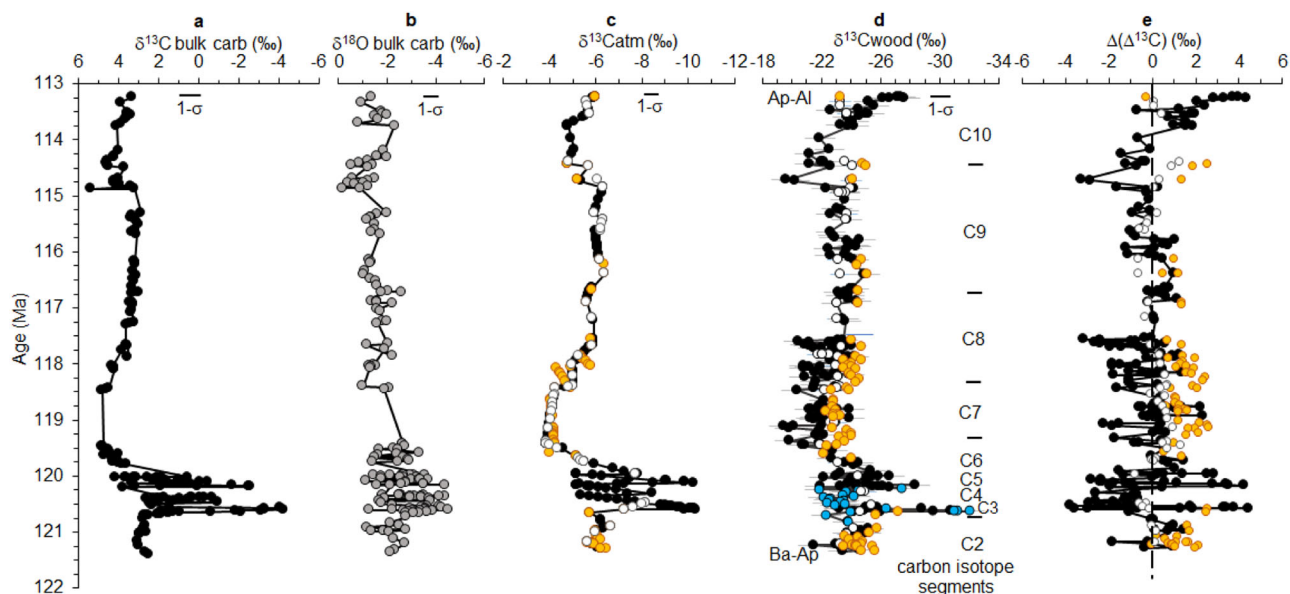


Fig. 3 | Data for computation of atmospheric CO₂ concentrations by the C₃ plant and $\Delta(\text{CIE}_{\text{wood}} - \text{CIE}_{\text{atm}})$ proxies during the Aptian. a $\delta^{13}\text{C}$ and (b) $\delta^{18}\text{O}$ values from bulk carbonate of DSDP 463 in the south equatorial Pacific^{55,56}. c $\delta^{13}\text{C}$ values of atmospheric CO₂ calculated from data panels (a, b) for the western Tethys (black)²², Svalbard (orange)²³, and Japan (white)²⁴. d Aptian $\delta^{13}\text{C}$ wood values from the three

study localities (turquoise symbols indicate potential marine influence in western Tethys) in relation to the carbon isotope segments C2–10 with same color coding as shown previously and in the next adjacent panel. e $\Delta(\delta^{13}\text{C})$ relative proxy for atmospheric CO₂ trends. All uncertainties computed by 10,000 Monte Carlo simulations (Supplementary Table 1). All values reported relative to PDB.

Wight in the western Tethys²², from Arctic Svalbard²³, and from Japan²⁴ (Fig. 2; Fig. 3d, e; Supplementary Data 3–5). The wood age model was first developed from the western Tethys stratigraphic section and correlated by key inflection points to the lower resolution $\delta^{13}\text{C}_{\text{atm}}$ curve from DSDP 463 (Supplementary Figs. 2–4). The geochronology of this $\delta^{13}\text{C}_{\text{atm}}$ record was then applied to the Svalbard and Japan localities from key inflection points to assign a $\delta^{13}\text{C}_{\text{atm}}$ value to each of those wood $\delta^{13}\text{C}$ values.

Wood from the western Tethys section was identified as *Cupressinoxylon vectense*, while the studies from Svalbard and Japan did not report wood type. However, chemostratigraphic alignment of the wood $\delta^{13}\text{C}$ curves from these three distinct geographical localities, as well as alignment with other terrestrial organic carbon $\delta^{13}\text{C}$ records (Supplementary Fig. 1), support a global atmospheric signal imparted during photosynthesis that is also expressed in the marine-based $\delta^{13}\text{C}_{\text{atm}}$ record (Fig. 3).

Moisture effects on the wood $\delta^{13}\text{C}$ values of *C. vectense* were considered to be minimal because tracheid diameters, which we measured from published micro-photographs²², were relatively large. Compared to modern gymnosperms, it indicates that annual rainfall at the western Tethys site during much of the Aptian was near 1500 mm (Supplementary Fig. 5; Supplementary Data 6), limiting the effect of water-deficit on the wood $\delta^{13}\text{C}$ values²⁵ to a few tenths of a permil. To further constrain the effects of different plant species and moisture effects on the C₃ plant proxy, we selected a modern datum with similar species to *C. vectense* (Supplementary Data 7).

The C₃ plant proxy was developed experimentally with a static O₂ concentration of 21%. We performed a theoretical calculation showing that differences in O₂ concentration during the Cretaceous had little effect on the $\delta^{13}\text{C}$ of wood in the study area (Methods, Supplementary Table 2). Because the adjustment was so small we did not apply an adjustment factor.

Using the C₃ plant proxy approach, CO₂ concentrations from the three wood localities are similar in magnitude and trend (Fig. 4a; Supplementary Data 8). The C2 isotopic segment prior to the OAE 1a from the western Tethys locality (~121.4–120.71 myrs) has a median of 547 ppm (273 to 1251). During the OAE 1a (C3–C6), four median CO₂ spikes are evident ranging from 1466 to 2302 ppm with 84th percentile values exceeding 3000 ppm. The median CO₂ is 612 ppm (227– > 3000 ppm) through C7

(120.71–118.45 myrs), which includes the Noir (Wezel) OAE. Carbon dioxide median concentrations decline further during C8 and C9 (118.45 to 114.73 myrs) to 491 ppm (206 to 1119 ppm) encompassing the Fallot and Nolan OAEs. The amplitude shifts from ~400 ppm near the base of C10 to nearly ~2200 ppm near the Aptian-Albian boundary (113.2 myrs) encompassing the Kilian OAE.

To assess whether these events occurred during a ‘background’ climate that was already warm, we estimated baseline CO₂ just prior to both the OAE 1a and prior to the end-Aptian by simultaneously solving for $\Delta(\text{CIE}_{\text{wood}} - \text{CIE}_{\text{atm}})$ through mass balance constraints. Here, it is assumed that a larger negative CIE in plants than in marine carbonates is due to a CO₂ effect on plant $\delta^{13}\text{C}$ values¹⁷ rather than to actual differences between the atmospheric and oceanic CIE, as the latter requires very rapid carbon input (i.e. 5 kyrs)²⁶. One advantage of this approach is that the calculated baseline CO₂ is primarily sensitive to $\Delta(\text{CIE}_{\text{wood}} - \text{CIE}_{\text{atm}})$, the value of which we know fairly well. For this approach (Supplementary Data 9), we selected the lowermost thirteen $\delta^{13}\text{C}$ data points on wood in the earliest Aptian (121.533 to 120.706 myrs) and compared to the CIE of the OAE 1 based on an average of the five most negative value from 120.628 to 120.637 and 120.640 to 120.649 myrs. The late Aptian included a group of eight data points through an interval with $\delta^{13}\text{C}$ values (114.730 to 113.897 myrs) and compared to the CIE average from the uppermost five data points at the end Aptian (Kilian) (113.243 to 113.265 myrs). These two groups of data points were selected because they represent relatively stable isotopic ratios preceding the two CIEs (Supplementary Data 3). Results suggest that when assuming a carbon source with a $\delta^{13}\text{C}$ value of $-17.5 \pm 5\text{‰}$ that spans the range of possible mantle and organic sources^{27,28}, along with a conversion factor of 0.1 from mass of carbon to atmospheric CO₂ (McInerney and Wing, 2011)²⁹, initial CO₂ would have been approximately 482 ppm prior to the OAE 1a (92% of values < 840 ppm) and approximately 215 ppm prior to the end Aptian OAE (100% of values less than 840 ppm) (Supplementary Data 9). These values align with the CO₂ curve produced by the C₃ plant proxy for their respective time intervals. If assuming a 2‰ enrichment in $\delta^{13}\text{C}$ of wood from moisture stress, atmospheric CO₂ is at the ice-free line in the early Aptian and still well within the ice sheet window during the late Aptian (Supplementary Data 9).

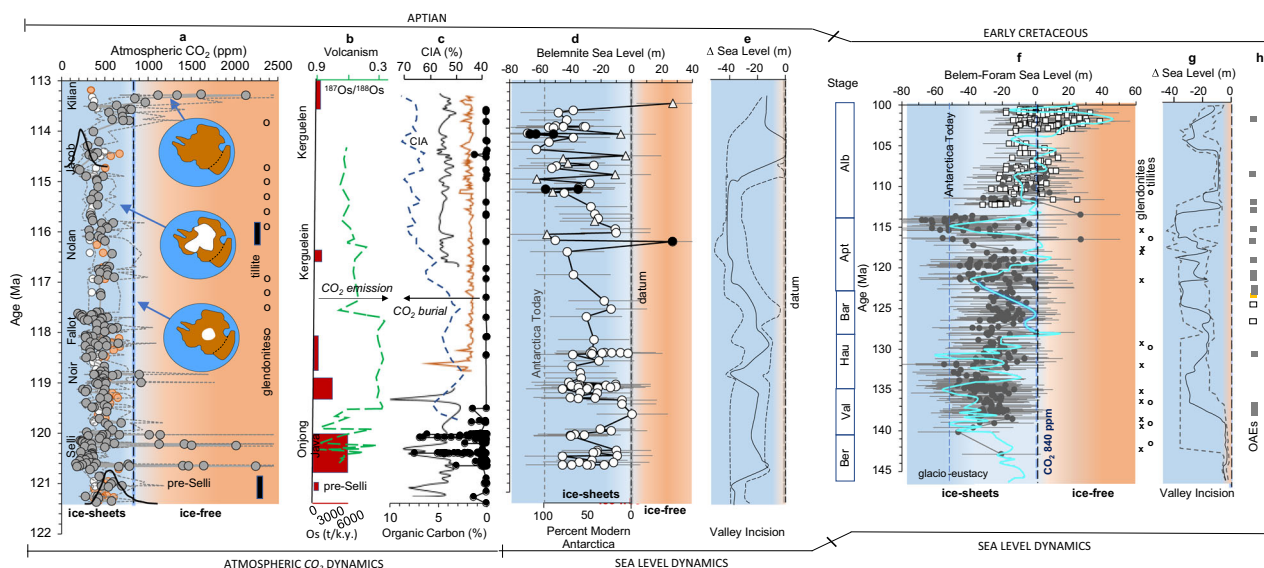


Fig. 4 | Indicators of Aptian and early Cretaceous climate. **a** Atmospheric CO₂ estimates from the C₃ plant proxy on wood from the western Tethys (16th and 84th percentile uncertainty), Svalbard (orange circles), and Japan (white circles) (Supplementary Data 8). Kernel density estimates for CO₂ calculated using the $\Delta(\text{CIE}_{\text{wood}} - \text{CIE}_{\text{atm}})$ mass balance approach shown in black curve that corresponds to the baseline prior to OAE1a and end Aptian. Global GCM simulations of Antarctic ice sheets at three CO₂ concentrations during cooling⁷. Tillites are from Australia⁷² and glendonites⁴ and OAEs²¹ from global records. **b** Volcanism from modeled Os inputs (red blocks)²⁹ and ¹⁸⁷Os/¹⁸⁸O ratios (green line)⁷⁴. **c** Organic carbon concentrations from the subtropical Pacific⁵⁵ (black circles), North Atlantic⁷⁵ (orange line), and Svalbard²³ (black solid line). CIA weathering index (black dashed line) from marine deposits in eastern China⁷⁶. **d** Sea level from $\delta^{18}\text{O}$ of belemnites (16th and 84th

percentile uncertainty) relative to the ice-free datum line: white circles, Western Tethys^{9,77}; white triangles, Australia⁶⁹; black circles, Antarctica^{67,68}. Ice volume as percent of modern Antarctica. **e** Median glacio-eustatic sea level changes (< 3 myrs cycles) (16th and 84th percentile uncertainty) mainly from valley incisions⁸. Early Cretaceous sea level record from $\delta^{18}\text{O}$ values of benthic foraminifera (white squares) from North Atlantic and southern high latitudes⁶⁴ and belemnites (black circles) from the western Tethys⁹ with 16th and 84th percentile uncertainty (Methods) (Supplementary Data 11). Superimposed backstripped sea level curve (turquoise)¹⁵ relative to the 0 m datum⁶⁵ (adapted from ref. 65). Distribution of glendonites⁴ (x) and tillites⁷² (circle). **g** Median short term sea level amplitudes from glacial-eustasy⁸. **h** Occurrence of OAEs^{21,78} and LIPs (brown⁷⁹, purple⁷⁸; yellow and red²¹; gradient fill^{80,81}).

Despite uncertainties associated with quantitative CO₂ estimates using both the C₃ plant proxy and the $\Delta(\text{CIE}_{\text{wood}} - \text{CIE}_{\text{atm}})$ approaches, a baseline Aptian CO₂ below the simulated threshold for polar ice sheets appears likely and is supported by the presence of tillites and glendonites during the earliest and late Aptian (Fig. 4a).

Atmospheric CO₂ dynamics

While the new Aptian curve presented here shows atmospheric CO₂ concentrations to be mainly below 840 ppm, it is punctuated by short-lived CO₂ pulses. During the Selli (OAE 1a) and possibly Noir (i.e. Wezel) OAEs of the early Aptian, and the Kilian OAE of the end-Aptian, CO₂ spikes point to warm snaps when concentrations were near or above 1000 ppm and ice sheets likely not present on Antarctica (Fig. 4a). Initiation of the Selli, and possibly the Noir, appears to have emanated from the Pacific Ontang-Java LIP (Fig. 2) because of unradiogenic sea water Os concentrations^{30,31} (Fig. 4b). Organic carbon abundances during this interval may have regulated background atmospheric CO₂ levels below 840 ppm, probably as a lagged response from continental weathering (Fig. 4c). Couplets of CO₂ release and subsequent drawdown occurred within 0.2 to 0.3 myrs after each event according to lithium isotopes ratios helping to explain the abrupt decline in CO₂ several times during the OAE 1a³¹.

Volcanic pulses were less intense after the Noir but may have contributed to the formation of the Nolan and Jacob OAEs associated with atmospheric CO₂ concentrations between 600 and 1200 ppm. During these intervals, organic carbon content in marine reservoirs had stabilized at lower, but detectable concentrations, apparently catalyzed by increased silicate weathering as measured through the CIA (chemical index of alteration) (Fig. 4c). This process apparently sustained CO₂ concentrations within the glacial window for millions of years during the middle to late Aptian until volcanism was reactivated near the end Aptian³⁰ as CO₂ concentrations increased by up to an order of magnitude.

Sea level

If ice sheets were present during the early Cretaceous, sea level would have fluctuated on short time scales reflecting a combination of orbital and tectonic forcing. To test this hypothesis, we reconstructed sea level based on $\delta^{18}\text{O}$ values of belemnites for the Aptian study area and on benthic foraminifera from the early Cretaceous Vocontian Basin. Here, first order sea level behavior follows the relative sea level concept (RSL) of transgressive and regressive marine phases as a proxy for global mean sea level where higher $\delta^{18}\text{O}$ values in sea water are more likely to be a response to the presence of ice sheets in polar regions³².

The sea level curves were constructed by taking the difference in either belemnites or benthic foraminifera between the $\delta^{18}\text{O}$ of a baseline value as the ice free line and other values through time, the rate change of $\delta^{18}\text{O}$ values to change in sea level, fractional contribution of glacially-derived water to the $\delta^{18}\text{O}$ values, and an isostatic adjustment factor (Methods; Supplementary Data 10).

Benthic foraminifera live deeper in the water column and are more likely to capture the full effect of polar-derived surface water tracking the ebb and flow of continental glaciers³³. For the Aptian, genera/species of belemnites⁹ were not reported but interpreted as reflecting deep water conditions in the Vocontian Basin. Cited from one study in this data base³⁴, the belemnites *Hibolithes* and *Neohibolithes* were abundant during the latter part of the Hauterivian through early Aptian that others interpret as outer shelf bottom water genera³⁵. The other belemnite $\delta^{18}\text{O}$ values used for sea level analysis reported in Fig. 4 from the Aptian were from the Antarctic realm. Thus, these data should largely carry a deep water isotopic signal capturing in ice sheet meltwater dynamics. This cold water observation is supported by the presence of glendonites poleward of 50° latitude in both hemispheres during the late Aptian that typically form in the ocean temperature range of 4–7 °C³⁶.

During the Aptian, sea level data points from this approach occur within the ice-sheet window, but range from brief periods of complete

melting to levels low enough to suggest the presence of ice sheets equivalent to that stored on Antarctica today. Low sea level based on $\delta^{18}\text{O}$ values is consistent with the global distribution of a cluster of the most deeply incised near-shore valleys suggesting fourth order orbital forcing (Fig. 4e). When the temporal resolution of the sea level data permits, the short-term fluctuations would best be explained by waxing and waning of ice sheets³⁷ even if aquifer- and thermal eustasy account for up to 10 m of sea level change³⁸.

Rapid sea level fluctuations evident in Fig. 1 suggest that the Aptian icehouse state may have been typical of other parts of the early Cretaceous. Our reconstruction of sea level curve for the early Cretaceous employed the same methods and assumptions from belemnites and benthic foraminifera as applied to the Aptian. Results show that early Cretaceous sea level was mainly below the ice-free datum (ice sheet realm), likely reflecting a similar atmospheric CO_2 range of < 840 ppm observed during the Aptian and supported in part from CO_2 proxy data and geochemical models (Fig. 4f; Supplementary Data 11). The short term sea level fluctuations through the study interval were typically on the order of 30 to 40 m. The lowest sea level was 60 and 70 m below datum during the late Aptian, while the highest estimates approached and then exceeding the 0 m datum line during the Albian. Glendonites and tillites are generally concentrated during intervals when sea level was lower, particularly during the Valanginian and Aptian, before disappearing in the Albian. Sea level rise during the Albian was possibly a response to widespread meltwater entering the ocean basins (~ 40 to 70 m) overwhelming the contributions from thermal eustasy, or perhaps in combination with rapid sea floor spreading and the reduction in size of ocean basins that began as early as the Aptian³⁹.

These proxy records correlate well both temporally and in magnitude with previous sea level estimates by sediment backstripping (e.g. adjustments in sediment loading, thermal subsidence, water depth) during the same time interval¹⁵ (Fig. 4f), and similarly with sea level shifts according to the frequency and magnitude of near-shore valley incisions⁸ (Fig. 4g). The error range on the backstripped sea level curve is estimated to be from 5 to 10 m, thus overlapping with the $\delta^{18}\text{O}$ -derived sea level curve presented here. Sediment backstripping suggests even lower sea level than our $\delta^{18}\text{O}$ -based estimates from 140 to 128 myrs. The sea level curve based on sequence stratigraphy¹⁴ suggests that sea level was 50 to 100 m higher than the $\delta^{18}\text{O}$ derived or backstripped-derived curves. However, the sequence stratigraphy approach does show a regressive phase during the Valanginian, transgression and then stability from the Hauterivian to middle Albian, and then another transgression during the late Albian (Figs. 1 and 4f). Furthermore, sea level shifts indicated in Figs. 1 and 4 imply that third and fourth order orbital forcing played a role in ice sheet dynamics during this time⁴⁰.

The documented LIP events constitute multiple short term shifts during much of the early Cretaceous record, which explains the presence of CO_2 pulses rather than sustained concentrations, especially in context of widespread and interspersed episodes of carbon burial from weathering on land (Fig. 4h). Together, these sea level records provide evidence for persistent to fluctuating ice sheets during the early Cretaceous on Antarctica, an interpretation of a colder climate state than previously thought.

Discussion

The new atmospheric CO_2 and sea level results reported here suggest that small to large ice sheets were commonly present on Antarctica, challenging the current paradigm that the early Cretaceous was part of a vast greenhouse climate state. This conclusion is drawn from two principal observations. First, is that during approximately three-fourths of the Aptian, CO_2 concentrations were within the theoretical glacial window of ≤ 840 ppm according to the C_3 plant proxy and CIE mass balance approach, and supported by the stomatal proxy and geochemical models. Second, are persistently low and rapidly fluctuating sea levels likely caused by ice sheets on Antarctica (Fig. 4).

Ice sheet coverage of more than half of Antarctica (2 km thick) during the Aptian at elevations of 1000 to 2000 m⁷ would have been equivalent to 30 to 50 m of eustatic sea level change^{32,41}, similar to our $\delta^{18}\text{O}$ -based reconstructions. Icehouse conditions during the Aptian were similar to the

Valanginian if comparing the amount of sea level fall and presence of glendonites and tillites, while the interval between appears to have been an intermediate state where orbital forcing brought sea level periodically closer to the ice-free sea level line. Melting of glaciers as evidenced by sea level rise marked the development of a true greenhouse state beginning in the Albian.

These findings alter our understanding of biotic migration and evolutionary patterns if ice existed in large masses for long intervals in polar regions. For example, during the Eocene-Oligocene transition, plant communities along the margins of Antarctica evolved from podocarp woodlands to tundra as a response to the presence of fluctuating glaciers on short time-scales⁴². This is similar to that observed on the margins of Antarctica during the Aptian⁴³, when ice sheets were likely present in the continental interior according to our data.

Moreover, it should not be surprising that $\delta^{18}\text{O}$ -derived temperatures on bone-derived meteoric waters were estimated to be 8 to 10 °C at a paleolatitude of 42° N (similar to today) in northwest China during parts of the early and late Aptian¹³. Temperature gradients would have been steeper and restricted crocodylian distribution to no more than 35° N latitude. In addition, exceptionally low $\delta^{18}\text{O}$ values on hydrothermal zircons suggest a glacial meltwater signal from similar latitudes⁴⁴.

The Aptian and early Cretaceous climate state was characterized by accelerating tectonic activity from the initial breakup of Pangea, the development of ocean anoxic events, and evolving biotic patterns⁴⁵. The proposed icehouse state during the early Cretaceous was apparently regulated by low level solid earth degassing interrupted by intense CO_2 pulses from hot spot/LIP activity mitigated by long lasting negative feedbacks from weathering and burial of carbon in evolving and sometimes isolated ocean basins. Given that these pulses waxed and waned, once CO_2 drawdown occurred, new pulses were vital to reform the ice-free state. These early Cretaceous warm snaps have influenced our conceptualization of climate and biology disproportionately to their duration. There is some evidence that ice sheets returned to Antarctica during the late Cretaceous³², although the extent and persistence appears to have been on the decline.

Invoking the early Cretaceous to model Earth's future climate and associated biota migration patterns and extinction events may be appropriate, not because it was a persistent greenhouse, but because significant parts of it represent an intermediate state of waxing and waning of small to large-size glaciers that would be expected as a transitional response to future global warming.

Methods

Aptian geochronology

The base of the Aptian begins with polarity chronozone M0r (121.4 myrs) and terminates at the top of the *Microhedbergelia miniglobularis* (approximately *Paraticinella rohrri*) planktonic foraminifera zone and the *Hypacanthoplites jacobi* Boreal ammonite zone (113.2 myrs)²¹. The OAE 1a spans mainly the upper half of the *Leupoldina cabri* planktonic foraminiferal zone in the Boreal realm and in the lower part of *Deshayesites deshayesi* in the Tethyan ammonite zone. We supplement the most recent geochronology where in addition to the ammonite zonation, the base of the C3 (CIE) isotopic segment is set to 0.750 myrs above the base of the Aptian with the C3-C6 isotopic segments (OAE 1a) assigned an interval of 1.1 myrs⁴⁶ (Supplemental Note 1). However, the chronological placement of the Aptian OAEs is somewhat different if based on recent astronomical tuning of the Aptian⁴⁷ even though the shifts in position of key events occur proportionally with time. The GTS 2020-based geochronology for the early Cretaceous was also taken from ammonites biozones and Stage boundaries to assign belemnite $\delta^{18}\text{O}$ ages to construct the sea level curve²¹.

C_3 plant isotope theory

Carbon isotope discrimination by C_3 plants during photosynthesis is estimated from $\Delta^{13}\text{C} = a + (b - a) \times C_i/C_a - f(\Gamma^*)/C_a$ where a is discrimination against ^{13}C from diffusion through plant stomata (4.4‰), b is discrimination at the carboxylation enzyme Rubisco (27–30‰), C_i and C_a are the concentrations of CO_2 in substomatal leaf cavities and the atmosphere

(< unity), and f (Γ^*)/Ca is photorespiration where f is the discrimination factor and Γ^* is the CO₂ compensation point partial pressure in absence of dark respiration⁴⁸.

Our rationale for using the C₃ plant proxy is based on the results of experimental work showing that, in the absence of moisture stress, isotopic fractionation of Ci is driven by atmospheric CO₂ (Supplementary Note 2). The C₃ plant proxy is based on recent chamber experiments, verifying that in the absence of photorespiration, the sensitivity of the proxy is at its highest at low external CO₂¹⁶ as plant stomatal conductance is increased to maximize CO₂ uptake. As CO₂ increases, the typical plant response is to reduce instantaneous stomatal conductance to conserve water loss, common in angiosperms but potentially less so in gymnosperms studied in this paper. Lower stomatal sensitivity to internal CO₂ changes observed in gymnosperms reduces the short-term physiological response of the plants to regulating Ci^{49,50}, thus increasing the likelihood of photosynthetic enzyme discrimination. Over longer time scales, studies show that adaptation by species changes maximum stomatal conductance, demonstrated by discrimination ($\delta^{13}C$) having increased in plants proportional to rising atmospheric CO₂ during the past 100 years⁵¹. This is due to variable plasticity in stomatal density and size expression among gymnosperms with changing CO₂^{52,53} and inherently low speciation rates (~0.2 per myrs) affecting anatomical changes on multi-million year times scales^{50,54}.

Input variables for the C₃ plant proxy

$\delta^{13}C$ of atmospheric CO₂. To compute the $\delta^{13}C_{atm}$ (Fig. 2c), bulk carbonate data was compiled from DSDP 463 in the open ocean south Pacific (~17°S) spanning carbon isotopic segments C2-C10^{55,56} (Supplementary Data 2). This data was used to estimate sea water temperature representative of the mixed photic zone by T (°C) = 17–4.52 ($\delta^{18}O_{cc} - \delta^{18}O_w$) + 0.03 ($\delta^{18}O_{cc} - \delta^{18}O_w$)², where $\delta^{18}O_w$ (SMOW) is assumed as –1‰ (ice-free) and $\delta^{18}O_{cc}$ (PDB) is bulk carbonate⁵⁷. These are provisional sea temperatures because of the possible presence of ice sheets, but that which has only a small influence on the computed $\delta^{13}C_{atm}$ ³⁶.

The $\delta^{13}C_{atm}$ values for the Aptian were then calculated from Eq. 1^{58,59} with the $\delta^{13}C$ of bulk carbonate and ¹⁸O-derived ocean temperatures from DSDP 463.

$$\delta^{13}C_{atm}(\text{‰}) = \left(\frac{\delta^{13}C_{cc} + \mathcal{E}_{DIC-CC} + 1000}{\mathcal{E}_{DIC-CO_2(g)} / 1000 + 1} \right) - 1000 \quad (1)$$

where $\delta^{13}C_{cc}$ follows the planktic foraminifera approach because bulk carbonate approximates similar sea water surface conditions. \mathcal{E}_{DIC-CC} and $\mathcal{E}_{DIC-CO_2(g)}$ are carbon isotope enrichment factors between dissolved inorganic carbon and calcite and between dissolved inorganic carbon and atmospheric CO₂, respectively. The former is set to –1‰ with the latter requiring additional steps, where

$$\begin{aligned} \mathcal{E}_{DIC-CO_2(g)} &= (0.91 \times \mathcal{E}HCO_3^- - CO_{2(g)}) + (0.08 \times \mathcal{E}CO_3^{2-} - CO_{2(g)}), \text{ and} \\ \mathcal{E}HCO_3^- - CO_{2(g)} &= -0.1411 \times T(\text{°C}) + 10.78, \text{ and} \\ \mathcal{E}CO_3^{2-} - CO_{2(g)} &= 0.052 \times T(\text{°C}) + 7.22 \end{aligned}$$

and T is temperature as described above.

Uncertainty was propagated through 10,000 iterations using an R Monte Carlo script for $\delta^{13}C_{atm}$ from the variables in Eq. 1 (Supplementary Table 1). Uncertainty was reported as a pooled standard deviation from error on each sample associated with the x and y axes of the transfer functions in the carbonate equilibrium reactions⁵⁹ and coupled with uncertainty on five stratigraphic beds from DSDP 463 having two or more samples with $\delta^{13}C$ and $\delta^{18}O$ measurements⁵⁵. The standard deviation for $\delta^{18}O_w$ was taken as 0.35‰ based on recent work from the modern hydrosphere showing an ice-free range of –1.24 to –0.89‰ from sea water³⁶. The sum of these uncertainties yielded a propagated standard deviation on $\delta^{13}C_{atm}$ of 0.56‰.

$\delta^{13}C$ wood. Two hundred and one fossil wood samples were reported from the western Tethys (Isle of Wight) identified mainly as *Cupressinoxylon vectense* (cypress-like conifer) and range from charcoaled to black and brown coals²² (Supplementary Data 3). The environment of deposition was shallow marine, and lagoonal to estuarine. An absolute age was assigned to each wood $\delta^{13}C$ value established by stage boundaries and ammonite biozones using GTS 2020 (Supplementary Notes 1, 2). We added 1.4‰ to each $\delta^{13}C$ value (from all three wood localities) based on findings showing that cellulose does not remain in wood after having been buried in deposits of Eocene age or older. Consequently, ¹³C-depleted lignins are believed to lower $\delta^{13}C$ values by 1.4‰ relative to preburial conditions⁶⁰. The effect of this adjustment yielded lower atmospheric CO₂ concentrations than without the adjustment when applied to the C₃ plant proxy. However, it does not affect the baseline CO₂ values $\Delta(CIE_{wood} - CIE_{atm})$ because the shifts are relative.

The $\delta^{13}C$ values of wood from Svalbard is part of the Barents Sea region located at a paleolatitude of ~78°N just off the northeast coast of Greenland during the Aptian²³. One hundred thirty nine wood samples were reported from claystones to sandstones in shallow marine shelf, prodeltas, and fluvial deltaic plains totaling ~45 m thick. The wood locality in central Japan is from the Ashibetsu area that stratigraphically consists of claystones to sandstones in shallow marine environments. A total of 46 $\delta^{13}C$ bulk samples were analyzed²⁴ with the organic fraction almost entirely of woody material (charcoaled wood with some cuticles, spore and/or pollen grains). The wood time scale created for the Isle of Wight was transferred to wood values at Svalbard and Japan by key inflection points (Supplementary Data 4, 5; Supplementary Note 2).

Atmospheric CO₂ computation

C₃ plant proxy. The input variables needed to compute CO₂ from the C₃ plant proxy are given in Supplementary Table 1. The difference between carbon isotopic fractionation during photosynthesis between the past $\Delta^{13}C_{(t)}$ and present $\Delta^{13}C_{(o)}$ is defined by:

$$\Delta(\Delta^{13}C) = \Delta^{13}C_{(t)} - \Delta^{13}C_{(o)} \quad (2)$$

This may be rewritten using the definition of discrimination as:

$$\Delta(\Delta^{13}C) = \frac{(\delta^{13}C_{atm(t)} - \delta^{13}C_{p(t)})}{(1 + \delta^{13}C_{p(t)}/1000)} - \frac{(\delta^{13}C_{atm(o)} - \delta^{13}C_{p(o)})}{(1 + \delta^{13}C_{p(o)}/1000)} \quad (3)$$

where $\delta^{13}C_{p(o)}$ and $\delta^{13}C_{atm(o)}$ are modern variables to compute $\Delta^{13}C_{(o)}$, and $\delta^{13}C_{p(t)}$ and $\delta^{13}C_{atm(t)}$ are parameters from the past to compute $\Delta^{13}C_{(t)}$.

The difference in $\Delta^{13}C_{(t)}$ and $\Delta^{13}C_{(o)}$ at each point determines the $\Delta(\Delta^{13}C)$. The departure of $\Delta^{13}C_{(t)}$ from $\Delta^{13}C_{(o)}$ is hypothesized to result from the effects of CO₂ concentration on carbon isotope fractionation¹⁶ where:

$$\Delta(\Delta^{13}C) = \frac{((A)(B)(CO_{2(t)} + C))}{((A + (B))(CO_{2(t)} + C))} - \frac{((A)(B)(CO_{2(o)} + C))}{((A + (B))(CO_{2(o)} + C))} \quad (4)$$

This equation can be rearranged to solve for atmospheric CO₂ concentration at any given point in time as:

$$\begin{aligned} \text{Atm CO}_{2(t=1)} &= (\Delta(\Delta^{13}C) * A^2 + \Delta(\Delta^{13}C) * A * B * CO_{2(t=0)} \\ &+ 2 * \Delta(\Delta^{13}C) * A * B * C + \Delta(\Delta^{13}C) * B^2 * C * CO_{2(t=0)} \\ &+ \Delta(\Delta^{13}C) * B^2 * C^2 + A^2 * B * CO_{2(t=0)}) / A^2 * B \\ &- \Delta(\Delta^{13}C) * A * B - \Delta(\Delta^{13}C) * B^2 * CO_{2(t=0)} - \Delta(\Delta^{13}C) * B^2 * C \end{aligned} \quad (5)$$

where A (28.26), B (0.22) and C (where it equals [4.4 x (A)] / [(A-4.4) x (B)]) are curve fitting parameters.

To compute $\Delta^{13}\text{C}_o$ in Eq. 2, wood $\delta^{13}\text{C}$ values from Pennsylvania and Wyoming sampled in 2009⁶¹ were combined with mean monthly $\delta^{13}\text{C}$ data of atmospheric CO_2 collected from Mauna Loa, Hawaii in the same year. The wood samples included Cupressaceae (*Taxodium*, *Metasequoia*) as nearest neighbor to *Cupressioxylon vectense* from the Isle of Wight²². The modern datum averaged $-24.63 \pm 0.78\text{‰}$ for wood, and $-8.30 \pm 0.11\text{‰}$ and 387.5 ± 0.30 ppm for atmospheric CO_2 (Supplementary Table 1).

Supplementary Table 1 lists the input variables for computation of uncertainties in the C_3 plant proxy. Uncertainty in the $\delta^{13}\text{C}_{\text{wood}(t)}$ comes from duplicate samples from nine layers through the stratigraphic section from the Isle of Wight (Supplementary Data 3). The pooled standard deviation is 0.77‰ and there is no trend in the standard deviation of the wood $\delta^{13}\text{C}$ comparisons, indicating independence of standard through and time. A, B, and C are curve fitting parameters with associated uncertainties in the parabolic relationship between atmospheric CO_2 and the $\Delta^{13}\text{C}$ of C_3 plants from growth chambers under controlled conditions at atmospheric O_2 of 21%. C is computed iteratively through the Monte Carlo simulations. The R script to compute the CO_2 values from the C_3 plant proxy was determined for 68% confidence intervals through 10,000 randomly drawn Monte Carlo iterations reporting the median and 16th and 84th percentiles on a Gaussian distribution¹⁶.

As a cross check to atmospheric CO_2 values determined from the C_3 plant proxy, we estimated initial (background) CO_2 concentrations prior to two positive CO_2 excursions (negative CIE) by performing a mass balance calculation¹⁷ where:

$$\Delta\text{CIE} = \frac{AB(\text{CO}_2\text{i} + C)}{(A + B(\text{CO}_2\text{i} + C)) - AB(\text{CO}_2\text{ex} + C)} / (A + B(\text{CO}_2\text{ex} + C)), \text{ and}$$

$\Delta\text{CO}_2 = \text{CO}_2\text{ex} - \text{CO}_2\text{i}$ and $A = 28.26$, $B = 0.21$, $C = 25$, $C = \text{mass of carbon (pg) for initial (i) and excursion (ex), and } \text{CO}_2 = \text{atmospheric } \text{CO}_2 \text{ concentration (ppm) for initial (i) and excursion (ex). These equations are solved simultaneously for } \text{CO}_2\text{i}$.

Uncertainty on the two CO_2 estimates, one from the early and one from the late Aptian, was determined by Monte Carlo error propagation of CO_2i values. During each of 10,000 iterations, input values were randomly selected from distributions assigned as follows. All input variables were assumed to be normal distributions except for the conversion factor between mass of carbon released and the ppm increase in atmospheric CO_2 . For this conversion factor, a uniform distribution from 0.05 to 0.1 was used^{28,29}. The distributions for $\delta^{13}\text{C}$ values of marine carbonate and atmospheric CO_2 ^{55,56}, and of wood²² were determined from previously reported data. The distribution for $\delta^{13}\text{C}$ values of source carbon was assigned as $-17 \pm 5\%$ (1 sigma) to account for sources ranging from mantle carbon to terrestrial organic matter. The distribution for initial mass of carbon was assigned such that 1 sigma was 10% of the best value (i.e., 50000 ± 5000 Pg).

Another factor that influences the atmospheric CO_2 output from the C_3 plant proxy is atmospheric oxygen concentration, because it was estimated at $\sim 26\%$ during the Aptian⁶². However, the C_3 plant proxy was established experimentally at a static O_2 concentration of 21%. We performed a theoretical calculation assessing the potential impact of elevated O_2 on atmospheric CO_2 (Supplementary Table 2). Results show that the impact on $\Delta(\Delta^{13}\text{C})$ is minimal between these two oxygen concentrations but would serve to slightly lower atmospheric CO_2 estimates using the C_3 plant proxy by 4 to 6‰ across a CO_2 range of 300 to 1200 ppm because higher O_2 increases the CO_2 compensation point, thus lowering $\Delta^{13}\text{C}$ (see footnote to Supplementary Table 2 and section on C_3 plant theory). We did not, however, make this adjustment to the CO_2 curve in Fig. 4a because it was small.

Sea level

The transfer function for relative sea level (SL) for the Aptian is $\text{SL} = \Delta^{18}\text{O}_{t-o} * 10 \text{ m}/0.1 * 0.5 * 0.68$, where $\Delta^{18}\text{O}_{t-o}$ is the difference in belemnite or benthic foraminifera $\delta^{18}\text{O}$ values between the ice-free state ($o = -1.01\text{‰}$ for belemnites and -0.64‰ for benthic foraminifera) and that measured at a particular point in time (t), 0.1 is the rate change of $\delta^{18}\text{O}$ per 10 m of sea level

calibrated to the Cretaceous³², 0.5 is the contribution of sea water from ice to the $\delta^{18}\text{O}$ of belemnites averaged between 0.33 proposed for benthic foraminifera³² from the late Cretaceous and 0.66‰ from the early Cretaceous proposed for belemnites⁹, and 0.68 as the isostatic adjustment factor¹⁸.

In a previous study for the late Cretaceous, the 0 m sea level line was set to -0.64‰ from deep water benthic foraminifera (adjusted to *Cibicidoides*)³². Belemnites represent water habitats near or below the thermocline (deeper than bulk carbonate organisms and possibly plankton)⁶³, making their contemporaneous $\delta^{18}\text{O}$ values more responsive to ocean waters influenced by ice sheets on land and less responsive to the surface effects of seasonal temperature, evaporation, and freshwater inputs.

While belemnites were deep water species in the Vocontian Basin during the early Cretaceous, the baseline sea level $\delta^{18}\text{O}$ value representing 0 m is likely lower (more negative) for belemnites than benthic foraminifera. A comparison of the $\delta^{18}\text{O}$ of belemnites and benthic foraminifera where they overlap between 107 and 114 myrs ago⁶⁴ revealed that the belemnite mean value was significantly lower than the benthic foraminifera mean value by 0.37‰. Thus, we subtracted this value from the -0.64‰ value used as the ice free line for benthic foraminifera to produce the ice free line for belemnites at -1.01‰ .

There is no uncertainty provided for the baseline benthic foraminifera value of -0.64‰ used for the 0 m sea level line³². However, the uncertainty of normalizing $\delta^{18}\text{O}$ values from benthic foraminifera (-0.64‰) to belemnites (-1.01‰) carries with it additional error of 0.59‰. This rather large value is used for sea level calculations from both benthic foraminifera and belemnites. The uncertainty on the measured belemnite $\delta^{18}\text{O}$ values (and assumed for benthic foraminifera) spanning the study interval is 0.35‰ based on paired samples from the stratigraphic interval (Supplementary Data 10, 11). The 0.1‰ ($\delta^{18}\text{O}$) per 10 m rate change in sea level has been used on benthic foraminifera during the Oligocene, and is therefore conservative because $\delta^{18}\text{O}$ values of ice were probably higher during the Cretaceous³². For this variable we assign an uncertainty of 10%, 0.01. The contributions of ice to the $\delta^{18}\text{O}$ value of belemnites is set to 0.5 with an uncertainty of 0.07 (14%). Uncertainties were propagated by 10,000 runs across all variables in the sea level computation using the R-statistical package to report the median and 16th and 84th percentiles.

Connecting of the sediment backstripping sea level curve developed on the stable Russian Platform¹⁵ to our $\delta^{18}\text{O}$ -based sea level curve is an approximation. Originally, the early to middle Cretaceous Russian Platform curve was matched to a late Cretaceous curve established from backstripping of the New Jersey Platform⁶⁵. Consequently, we used the Russian platform sea level curve relative to 0 m as reported in the New Jersey study. While it has been argued that the New Jersey Platform sea level curve should be adjusted upward to account for subsidence¹⁴ (see Haq, 2014), there is no indication that an adjustment is needed for the Russian Platform curve. Even though there is some uncertainty in placement of the Russian platform sea level curve it mimics the $\delta^{18}\text{O}$ -derived sea level curve in our study in both space and time. The uncertainty of that sea level curve was estimated during our study interval to range between 5 and 10 m.

Groundwater storage and thermal eustasy are believed by some to have forced sea level shifts by up to 50 m⁶⁶. However, the former would require nearly instantaneous filling and emptying of all groundwater reservoirs and the latter would require unrealistically high temperatures to raise sea level above 5 m⁸. The assumption has been that in response to elevated CO_2 , the hydrological cycle quickens and leads to storage of groundwater mitigating eustatic sea level rise, and vice versa for low CO_2 . However, recent GCM simulations show that groundwater reservoirs may fill more during cooler intervals (more arid) amplifying a fall in sea level from glacio-eustasy by up to 5 m that in concert with thermal eustasy from cooling, contributes to short term sea level changes by up to 10 m³⁸. Accordingly, our sea level results may overestimate low stands by this amount, but this is more than offset by our using an isostatic adjustment factor of 0.68 when based on ice volume calculations excluding density effects on ocean basins from meltwater³⁷.

Data availability

The Supplementary Information and Supplementary Data files as supporting evidence for our conclusions are deposited in the Texas Data Repository at <https://doi.org/10.18738/T8/R4WH4Z>.

Received: 6 September 2023; Accepted: 12 April 2024;

Published online: 27 April 2024

References

- Kidder, D. L. & Worsely, R. R. Phanerozoic large igneous provinces (LIPs), HEATT (Halie Euxinic Acidic Thermal Transgression) episodes, and mass extinctions. *Palaeogeogr., Palaeoclimatol., Palaeoecol.* **295**, 162–191 (2010).
- Huber, B. T., MacLeod, K. G., Watkins, D. K. & Coffin, M. F. The rise and fall of the Cretaceous hot greenhouse climate. *Glob. Planetary Change* **167**, 1–23 (2018).
- Scotese, C. R., Song, H., Mills, B. J. W. & van der Meer, D. G. Phanerozoic paleotemperatures: The earth's changing climate during the last 540 million years. *Earth-Sci. Rev.* **215**, 103503 (2021).
- Rogav, M. et al. Database of global glendonite and iaitite records throughout the Phanerozoic. *Earth Sys. Sci. Data* **13**, 343–356 (2021).
- Cavalheiro, L. et al. Impact of global cooling on Early Cretaceous high pCO₂ world during the Weissert Event. *Nat. Commun.* **12**, 5411 (2021).
- Price, G. D. The evidence and implications of polar ice during the Mesozoic. *Earth-Sci. Rev.* **48**, 183–210 (1999).
- Ladant, J.-B. & Donnadieu, Y. Palaeogeographic regulation of glacial events during the Cretaceous supergreenhouse. *Nat. Commun.* **7**, 12771 (2016).
- Ray, D. C. et al. The magnitude and cause of short-term eustatic Cretaceous sea-level change: A synthesis. *Earth-Sci. Rev.* **197**, 102901 (2019).
- Bodin, S., Meissner, P., Janssen, N. M. M., Steuber, T. & Mutterlose, J. Large igneous provinces and organic carbon burial: Controls on global temperature and continental weathering during the Early Cretaceous. *Glob. Planetary Change* **133**, 238–253 (2015).
- Foster, G. L., Royer, D. L. & Lunt, D. J. Future climate forcing potentially without precedent in the last 420 million years. *Nat. Commun.* **8**, 14845 (2017).
- Royer, D. L. et al. Error analysis of CO₂ and O₂ estimates from the long-term geochemical model GEOCARBSULF. *Am. J. Sci.* **314**, 1259–1283 (2014).
- Lenton, T. M., Daines, S. J. & Mills, B. J. W. COPSE reloaded: An improved model of biogeochemical cycling over Phanerozoic time. *Earth-Sci. Rev.* **178**, 1–28 (2018).
- Amiot, R. et al. Oxygen isotopes of East Asian dinosaurs reveal exceptionally cold Early Cretaceous climates. *Proc. Natl. Acad. Sci.* **108**, 5179–5183 (2011).
- Haq, B. Cretaceous eustasy revisited. *Glob. Planetary Change* **113**, 44–58 (2014).
- Sahagian, D., Pinous, O., Olfieriev, A. & Zakharov, V. Eustatic curve for the Middle Jurassic–Cretaceous based on Russian Platform and Siberian stratigraphy: Zonal resolution. *AAPG Bull.* **80**, 1433–1458 (1996).
- Cui, Y. & Schubert, B. A. Quantifying uncertainty of the past pCO₂ determined changes in C₃ plant carbon isotope fractionation. *Geochimica et Cosmochimica Acta* **172**, 127–138 (2016).
- Schubert, B. A. & Jahren, A. H. Reconciliation of marine and terrestrial carbon isotope excursions based on changing atmospheric CO₂ levels. *Nature Communications* **4**, 1653 (2013).
- Nordt, L., Breecker, D. & White, J. Jurassic ice-sheet fluctuations sensitive to atmospheric CO₂ dynamics. *Nature Geoscience* **15**, 54–59 (2021).
- Lomax, B. H., Lake, J. A., Leng, M. J. & Jardine, P. E. An experimental evaluation of the use of Δ¹³C as a proxy for palaeoatmospheric CO₂. *Geochim. et Cosmochim. Acta* **227**, 162–174 (2019).
- Mora, G., Carmo, A. M. & Elliot, W. Homeostatic response of Aptian gymnosperms to changes in atmospheric CO₂ concentrations. *Geology* **49**, 703–707 (2021).
- Gale, A. S., Mutterlose, J. & Batenburg, S. The Cretaceous Period. In *Geologic Time Scale 2020*, Vol. 2, p. 1023–1086 (Elsevier, 2020).
- Gröcke, D. R. The carbon isotope composition of ancient CO₂ based on higher-plant organic matter. *Philosophical Transac. Royal Soc.* **360**, 633–658 (2002).
- Vickers, M. L., Price, G. D., Jerrett, R. M. & Watkinson, M. Stratigraphic and geochemical expression of Barremian–Aptian global climate change in Arctic Svalbard. *Geosphere* **12**, 1594–1605 (2016).
- Ando, A., Kakegawa, T., Takashima, R. & Saito, T. Stratigraphic carbon isotope fluctuations of detrital woody materials during the Aptian Stage in Hokkaido, Japan: Comprehensive δ¹³C data from four sections of the Ashibetsu area. *J. Asian Earth Sci.* **21**, 835–847 (2003).
- Diefendorf, A. F., Mueller, K. E., Wing, S. L., Koch, P. L. & Freeman, K. H. Global patterns in leaf ¹³C discrimination and implications for studies of past and future climate. *Proc. Natl. Acad. Sci.* **107**, 5738–5743 (2010).
- Kirtland Turner, S. & Ridgwell, A. Development of a novel empirical framework for interpreting geological carbon isotope excursions, with implications for the rate of carbon injection across the PETM. *Earth Planetary Sci. Lett.* **435**, 1–13 (2016).
- Lee, H. et al. Incipient rifting accompanied the release of subcontinental lithospheric mantle volatiles in the Magadi and Natron basin, East Africa. *J. Volcanol.* **346**, 118–133 (2017).
- Adloff, M. et al. Unravelling the sources of carbon emissions at the onset of Oceanic Anoxic Event (OAE) 1a. *Earth Planetary Sci. Lett.* **530**, 115947 (2020).
- McInerney, F. & Wing, S. L. The Paleocene-Eocene Thermal Maximum: A perturbation of carbon cycle, climate, and biosphere with implications for the future. *Ann. Rev. Earth Planetary Sci.* **39**, 489–516 (2011).
- Matsumoto, H. et al. Marine Os isotopic evidence for multiple volcanic episodes during the Cretaceous Oceanic Anoxic Event 1b. *Scientific Rep.* **10**, 12601 (2020).
- Lechler, M., von Strandmann, P. A. E. P., Jenkyns, H. C., Prosser, G. & Parente, M. Lithium-isotope evidence for enhanced silicate weathering during OAE 1a (Early Aptian Selli event). *Earth Planetary Sci. Lett.* **432**, 210–222 (2015).
- Miller, K. G., Wright, J. D. & Browning, J. V. Visions of ice sheets in a greenhouse world. *Marine Geol.* **217**, 215–231 (2005).
- Cramer, B. S., Miller, K. G., Barrett, P. J. & Wright, J. D. Late Cretaceous–Neogene trends in deep ocean temperature and continental ice volume: Reconciling records of benthic foraminiferal geochemistry (δ¹⁸O and Mg/Ca) with sea level history. *J. Geophys. Res.* **116**, C12023 (2011).
- Mutterlose, J., Bottini, C., Schouten, S. & Damstè, J. S. S. High sea-surface temperatures during the early Aptian Oceanic Anoxic Event 1a in the Boreal Realm. *Geology* **42**, 439–442 (2014).
- Wang, T. et al. Early Cretaceous climate for the southern Tethyan Ocean: Insights from the geochemical and paleoecological analyses of extinct cephalopods. *Glob. Planetary Change* **229**, 104220 (2023).
- O'Brien, C. L. et al. Cretaceous sea-surface temperature evolution: Constraints from TEX₈₆ and planktonic foraminiferal oxygen isotopes. *Earth-Sci. Rev.* **172**, 224–247 (2017).
- Miller, K. G. et al. Cenozoic sea-level and cryospheric evolution from deep-sea geochemical and continental margin records. *Sci. Adv.* **6**, eaaz1346 (2020).
- Davies, A. et al. Assessing the impact of aquifer-eustasy on short-term Cretaceous sea-level. *Cretaceous Res.* **112**, 104445 (2020).
- Seton, M., Gaina, C., Müller, R. D. & Heine, C. Mid-Cretaceous seafloor spreading pulse: fact or fiction? *Geology* **37**, 687–690 (2009).
- Matthews, R. K. & Frohlich, C. Maximum flooding surfaces and sequence boundaries: comparison between observation and orbital

- forcing in the Cretaceous and Jurassic (65–190 Ma). *GeoArabia* **7**, 503–538 (2002).
41. Ladant, J.-B., Donnadiou, Y., Lefevre, V. & Dumas, C. The respective role of atmospheric carbon dioxide and orbital parameters on ice sheet evolution at the Eocene–Oligocene transition. *Paleoceanography* **29**, 810–823 (2014).
 42. Truswell, E. M. & MacPhail, M. K. Polar forest on the edge of extinction: what does the fossil spore and pollen evidence from East Antarctica say? *Australian Sys. Botany* **22**, 57–106 (2009).
 43. Poole, I. & Cantrill, D. J. Cretaceous and Cenozoic vegetation of Antarctica integrating the fossil wood record. *Geol. Soc., London, Special Publication* **258**, 63–81 (2006).
 44. Yang, W.-B. et al. Isotopic evidence for continental ice sheet in mid-latitude regions in the supergreenhouse Early Cretaceous. *Sci. Rep.* **3**, 2732 (2013).
 45. Föllmi, K. B. Early Cretaceous life, climate and anoxia. *Cretaceous Res.* **35**, 230–257 (2012).
 46. Jenkyns, H. C. Transient cooling episodes during Cretaceous Oceanic Anoxic Events with special reference to OAE 1a (Early Aptian). *Philosophical Transac. Royal Soc. A* **376**, 20170073 (2018).
 47. Leandro, C. G. et al. Astronomical tuning of the Aptian stage and its implications for age recalibrations and paleoclimatic events. *Nat. Commun.* **13**, 2941 (2020).
 48. Farquhar, G. D. & Wong, S. C. An empirical model of stomatal conductance. *Australian J. Plant Physiol.* **11**, 191–210 (1982).
 49. Voelker, S. L. A dynamic leaf gas-exchange strategy is conserved in woody plants under changing ambient CO₂: evidence from carbon isotope discrimination in paleo and CO₂ enrichment studies. *Glob. Change Biol.* **22**, 889–902 (2016).
 50. Klein, T. & Ramon, U. Stomatal sensitivity to CO₂ diverges between angiosperm and gymnosperm tree species. *Func. Ecol.* **33**, 1411–1424 (2019).
 51. Keeling, R. F. et al. Atmospheric evidence for a global secular increase in carbon isotopic discrimination of land photosynthesis. *Proc. Natl. Acad. Sci.* **114**, 10361–10366 (2017).
 52. Haworth, M., Heath, J. & McElwain, J. C. Differences in the response sensitivity of stomatal index to atmospheric CO₂ among four genera of Cupressaceae conifers. *Ann. Botany* **105**, 411–418 (2005).
 53. Porter, A. S., Yiotis, C., Montañez, I. P. & McElwain, J. C. Evolutionary differences in $\Delta^{13}\text{C}$ detected between spore and seed bearing plants following exposure to a range of atmospheric O₂:CO₂ ratios: implications for paleoatmosphere reconstruction. *Geochim. et Cosmochim. Acta* **213**, 517–533 (2020).
 54. Condamine, F. L., Silvestro, D., Koppelhus, E. B. & Antonelli, A. The rise of angiosperms pushed conifers to decline during global cooling. *Proc. Natl. Acad. Sci.* **117**, 28867–28875 (2020).
 55. Price, G. D. New constraints upon isotope variation during the early Cretaceous (Barremian–Cenomanian) from the Pacific Ocean. *Geol. Magazine* **140**, 513–522 (2003).
 56. Ando, A., Kaiho, K., Kawahata, H. & Kakegawa, T. Timing and magnitude of early Aptian extreme warming: Unraveling primary $\delta^{18}\text{O}$ variation in indurated pelagic carbonates at Deep Sea Drilling Project Site 463, central Pacific Ocean. *Palaeogeogr., Palaeoclimatol., Palaeoecol.* **260**, 463–476 (2008).
 57. Erez, J. & Luz, B. Experimental paleotemperature equation for planktonic foraminifera. *Geochim. et Cosmochim. Acta* **47**, 1025–1031 (1983).
 58. Tipple, B. J., Meyers, S. R. & Pagani, M. Carbon isotope ratio of Cenozoic CO₂: A comparative evaluation of available geochemical proxies. *Paleoceanography* **25**, PA3202 (2010).
 59. Zhang, J., Quay, P. D. & Wilbur, D. O. Carbon isotope fractionation during gas-water exchange and dissolution of CO₂. *Geochim. et Cosmochim. Acta* **59**, 107–114 (1995).
 60. Lukens, W. E., Eze, P. & Schubert, B. A. The effect of diagenesis on carbon isotope values of fossil wood. *Geology* **47**, 987–991 (2019).
 61. Diefendorf, A. F., Freeman, K. H., Wing, S. L. & Graham, H. V. Production of *n*-alkyl lipids in living plants and implications for the geologic past. *Geochim. et Cosmochim. Acta* **75**, 7472–7485 (2011).
 62. Krause, A. J. et al. Stepwise oxygenation of the Paleozoic atmosphere. *Nat. Commun.* **9**, 4081 (2020).
 63. Mutterlose, J., Malkoč, M., Schouten, S., Damsté, J. S. S. & Forster, A. TEX₈₆ and stable $\delta^{18}\text{O}$ paleothermometry of early Cretaceous sediments: Implications for belemnite ecology and paleotemperature proxy application. *Earth Planetary Sci. Lett.* **298**, 286–298 (2010).
 64. Friedrich, O., Norris, R. D. & Erbacher, J. Evolution of middle to Late Cretaceous oceans – 55 m.y. record of Earth’s temperature and carbon cycle. *Geology* **40**, 107–110 (2012).
 65. Miller, K. et al. The Phanerozoic Record of Global sea-level change. *Science* **310**, 1293–1298 (2005).
 66. Cloetingh, S. & Haq, B. U. Inherited landscapes and sea level change. *Science* **347** <https://doi.org/10.1126/science.1258375> (2015).
 67. Dorman, B. F. & Gill, E. D. Oxygen isotope palaeotemperature measurements on Australian fossils. *Proc. Royal Soc. Victoria* **71**, 73–98 (1959).
 68. Ditchfield, P. W., Marshall, J. D. & Pirrie High latitude palaeotemperature variation: New data from the Tithonian to Eocene of James Ross Island, Antarctica. *Palaeogeogr. Palaeoclimatol., Palaeoecol.* **107**, 79–101 (1994).
 69. Price, G. D., Twitchett, R. J., Wheeley, J. R. & Buono, G. Isotopic evidence for long term warmth in the Mesozoic. *Scientific Reports* **3**, 1438 (2013).
 70. Boucot, J., Hu, C. & Scotese, C. *Phanerozoic Paleoclimate: An Atlas of Lithologic Indicators of Climate* Vol. 11, p. 214–231 (SEPM Concepts in Sedimentology and Paleontology, Tulsa, OK, 2013). <https://doi.org/10.2110/sepmcsp.11.214>.
 71. Shaviv, N. J. & Veizer, J. Celestial driver of Phanerozoic climate. *GSA Today* **15**, 4–10 (2003).
 72. Alley, N. F., Hore, S. B. & Frakes, L. A. Glaciations at high-latitude Southern Australia during the Early Cretaceous. *Australian J. Earth Sci.* <https://doi.org/10.1080/08120099.2019.1590457> (2019).
 73. Rodríguez-López et al. Glacial dropstones in the western Tethys during the late Aptian–early Albian cold snap: Palaeoclimate and palaeogeographic implications of the mid-Cretaceous. *Palaeogeogr., Palaeoclimatol., Palaeoecol.* **452**, 11–27 (2016).
 74. Martínez-Rodríguez, R. et al. Tracking magmatism and oceanic change through the early Aptian Anoxic Event (OAE 1a) to the late Aptian: Insights from osmium isotopes from the westernmost Tethys (SE Spain) Cau Core. *Glob. Planetary Change* **207**, 103652 (2021).
 75. McAnena, A., et al., Atlantic cooling associated with the marine biotic crisis during the mid-Cretaceous period. *Nat. Geosci.* **6** <https://doi.org/10.1038/NGEO1850> (2013).
 76. Jia, J., Miao, C. & Xie, W. Terrestrial paleoclimate transition associated with continental weathering and drift during the Aptian–Albian of East Asia. *Geol. Soc. Am. Bull.* **135**, 467–480 (2021).
 77. Podlaha, O. G., JMutterlose, J. & Veizer, J. Preservation of $\delta^{18}\text{O}$ and $\delta^{13}\text{C}$ in belemnite rostra from the Jurassic/Early Cretaceous successions. *Am. J. Sci.* **298**, 324–347 (1998).
 78. Charbonnier, G. & Föllmi, K. B. Mercury enrichments in lower Aptian sediments support the link between Ontong Java large igneous province activity and oceanic anoxic episode 1a. *Geology* **45**, 63–66 (2017).
 79. Weissert, H. & Erba, E. Volcanism, CO₂ and palaeoclimate: a late Jurassic–Early Cretaceous carbon and oxygen isotope record. *J. Geol. Soc., London* **161**, 695–702 (2004).
 80. Kanchuk, A. I., Grebennikov, A. V. & Ivanov, V. V. Albian–Cenomanian orogenic belt and igneous province of Pacific Asia. *Russian J. Pacific Geol.* **13**, 187–219 (2019).
 81. Fan, Q., Xu, Z., MacLeod, K. G., Brumsack, A. V. & Li, T. First record of Oceanic Anoxic Event 1d at southern high latitudes: sedimentary and geochemical evidence from International Ocean Discovery Program Expedition 369. *Geophys. Res. Lett.* **49**, e2021GL097641 (2022).

Acknowledgements

We thank the editors and four anonymous reviewers for suggestions that improved the clarity of the manuscript. We also thank Stéphane Bodin for kindly providing his published $\delta^{18}\text{O}$ belemnite data from the Vocontian Basin.

Author contributions

All authors participated jointly in the research design of the study, including data analysis and interpretation. L.N. contributed mainly to the C_3 plant proxy CO_2 and sea level computations, D.B. to the CO_2 CIE mass balance computations and J.W. to C_3 plant physiology interpretations.

Competing interests

The authors declare no competing interests.

Additional information

Supplementary information The online version contains supplementary material available at <https://doi.org/10.1038/s43247-024-01389-5>.

Correspondence and requests for materials should be addressed to Lee Nordt.

Peer review information *Communications Earth and Environment* thanks the anonymous reviewers for their contribution to the peer review of this

work. Primary Handling Editors: Sze Ling Ho, Alireza Bahadori and Aliénor Lavergne. A peer review file is available.

Reprints and permissions information is available at <http://www.nature.com/reprints>

Publisher's note Springer Nature remains neutral with regard to jurisdictional claims in published maps and institutional affiliations.

Open Access This article is licensed under a Creative Commons Attribution 4.0 International License, which permits use, sharing, adaptation, distribution and reproduction in any medium or format, as long as you give appropriate credit to the original author(s) and the source, provide a link to the Creative Commons licence, and indicate if changes were made. The images or other third party material in this article are included in the article's Creative Commons licence, unless indicated otherwise in a credit line to the material. If material is not included in the article's Creative Commons licence and your intended use is not permitted by statutory regulation or exceeds the permitted use, you will need to obtain permission directly from the copyright holder. To view a copy of this licence, visit <http://creativecommons.org/licenses/by/4.0/>.

© The Author(s) 2024